Chemical Science

ROYAL SOCIETY OF CHEMISTRY

EDGE ARTICLE

View Article Online
View Journal | View Issue

Cite this: *Chem. Sci.*, 2025, **16**, 7495

All publication charges for this article have been paid for by the Royal Society of Chemistry

Received 23rd February 2025
Accepted 17th March 2025

DOI: 10.1039/d5sc01439e

rsc.li/chemical-science

Narrowband multi-resonance pure-red emitters *via* enhanced molecular orbital delocalization for high-performance organic light-emitting diodes†

Xiaowei Wang,‡[a] Tao Hua,‡*[ab] Nengquan Li,[a] Guohao Chen,[a] Zhanxiang Chen,[a] Jingsheng Miao,[a] Xiaosong Cao[a] and Chuluo Yang*[a]

Multiple resonance-induced thermally activated delayed fluorescence (MR-TADF) materials with pure-red gamut are in demand for high-definition organic light-emitting diode (OLED) displays. To achieve efficient pure-red OLEDs with excellent color purity, we report three novel MR-TADF emitters: **PhCzBN**, **PhBCzBN**, and **BCzBN**, which integrate a dibenzo[*c*,*g*]carbazole segment into a para-boron/oxygen-embedded framework, resulting in the progressive extension of the molecular conjugation. This extension of the π-conjugated skeleton enhances frontier molecular orbital (FMO) delocalization and red-shifts the emission, yielding pure-red emission in toluene with satisfactory peak positions and narrow linewidths. The sensitized OLEDs incorporating **PhCzBN**, **PhBCzBN**, and **BCzBN** exhibit maximum external quantum efficiencies of 31.5%, 33.6%, and 33.8%, respectively. The current efficiencies of these devices reach as high as 42.5 cd A^{-1}, which is higher than reported pure-red emitters with comparable CIE coordinates. Notably, the devices based on **BCzBN** demonstrate an emission peak at 636 nm and superior CIE coordinates of (0.700, 0.300), closely aligning with the BT.2020 requirements for the red gamut. This work presents a straightforward yet effective approach for developing high-performance pure-red MR-TADF OLEDs, marking a substantial advancement in wide-color gamut display technologies.

Introduction

Organic light-emitting diodes (OLEDs) have attracted significant attention due to their numerous attractive advantages in display and lighting technologies. With the rapid proliferation of smart phones, automobiles, and other devices, the benefits of smaller OLED screens become even more pronounced.[1] As demand for ultra-high-definition (UHD) displays, the color gamut standard has been elevated to the Broadcast Service Television 2020 (BT.2020) requirement, underscoring the need for advanced OLED technologies.[2] This stringent standard emphasizes significantly improving the Commission Internationale de l'Eclairage (CIE) coordinates for red, green, and blue colors. Superior CIE coordinates need to achieve both a suitable spectral peak and a narrow full width at half maximum (FWHM).[3] To tackle the challenge of FWHM, Hatakayama *et al.* developed a new class of luminescent materials known as multiple resonance-induced thermally activated delayed fluorescence (MR-TADF) materials.[4] These materials feature a rigid architecture with alternating electron-donating and electron-withdrawing distributions, which effectively minimize the bonding/antibonding characters between adjacent atoms. As a result, structural relaxation and vibrational coupling in MR-TADF emitters are remarkably suppressed, leading to minimal structural displacement and a highly sharp fluorescence emission spectrum.[5]

The distinctive spectral features of MR-TADF materials make them ideal for use as light-emitting layers in OLEDs, fulfilling the requirements of UHD visuals without the need for additional color filters or optical microcavities.[6] MR-TADF materials based on boron/nitrogen (B/N) heteroaromatic skeletons have atomically separated highest occupied molecular orbitals (HOMO) and lowest unoccupied molecular orbitals (LUMO) due to the alternating positions of B and N atoms. This distribution of frontier molecular orbitals (FMOs) leads to short-range charge transfer (SR-CT) and a reasonable singlet (S_1)–triplet (T_1) energy gap (ΔE_{ST}), which is responsible for the TADF characteristic.[7] Despite the significant advancements made in high-efficiency blue and green MR-TADF emitters with exceptional color purity,[8] as one of the three primary colors, the electroluminescent (EL) performance of red MR-TADF devices, which concurrently meet the high EL performance and the CIE

[a]*Shenzhen Key Laboratory of New Information Display and Storage Materials, College of Materials Science and Engineering, Shenzhen University, Shenzhen 518060, P. R. China. E-mail: clyang@szu.edu.cn*

[b]*Institute of Technology for Future Industry, School of Science and Technology, Instrument Application Engineering, Shenzhen Institute of Information Technology, Shenzhen, 518172, P. R. China. E-mail: taohua@sziit.edu.cn*

† Electronic supplementary information (ESI) available. CCDC 2373696. For ESI and crystallographic data in CIF or other electronic format see DOI: https://doi.org/10.1039/d5sc01439e

‡ These authors contributed equally.

coordinates, is still far from the requirement of UHD displays. Under the BT.2020 standard, prime red emitters for pure-red OLEDs should satisfy CIE coordinates of (0.708, 0.292), corresponding to a monochromatic light wavelength of ~630 nm. The emission peak position and FWHM are recognized as two critical factors for achieving high color purity. However, designing high-efficiency pure-red MR-TADF emitters with appropriate spectral peaks is challenging due to limited structural modifications of the polycyclic aromatic hydrocarbon (PAH) skeleton. The primary strategies involve enhancing the charge transfer (CT) process and extending multiple fusion π-skeletons.[9] However, these approaches often lead to large molecular weights, complicated synthetic routes, and low yields, posing challenges to vacuum deposition applications. Recent research has shifted towards integrating *para*-boron (B–π–B) into the PAH framework. This modification improves electronic coupling and facilitates the formation of constrained π-bonds within the phenyl core, resulting in a narrower energy gap and a significant red shift in emission, albeit with a slight reduction in the multiple resonance effect.[10] Based on this strategy, Yasuda *et al.* developed a red MR-TADF emitter of BBCz-R, and the corresponding OLED exhibited an emission peak at 616 nm with a narrow FWHM of 26 nm.[11] Duan's group has made substantial strides in developing pure-red MR-TADF emitters by incorporating 5-phenyl-5,8-dihydroindolocarbazole as multiple nitrogen sources into the B/O MR skeleton, achieving pure-red emission with an emission wavelength of 643 nm and a narrow FWHM of 42 nm.[12] Our group has also conducted systematic studies in this field.[13] For example, we reported a class of red MR emitters (BNO1-3) by inserting oxygen atoms into *bis*-boron-based frameworks with *para*-B–π–B and N–π–N structures. These devices achieved an external quantum efficiency (EQE) as high as 36.1%. However, their CIE coordinates (0.66, 0.34) fall short of the BT.2020 standard. To achieve stringent CIE coordinates for BT.2020 red color, we developed a series of *bis*-boron-based MR-TADF emitters by integrating large building block motifs with heteroatoms.[14] However, this approach resulted in a pronounced shift and a deep-red emission with maximum emission peaks at 693 and 671 nm. While the targeted CIE coordinates were achieved, the enhancement in the deep-red and near-infrared regions, where human eye sensitivity markedly decreases, led to severe and imperceptible energy losses, particularly impacting current efficiency (CE). CE plays a crucial role in determining the energy consumption and luminous performance of OLEDs. A higher CE enables OLEDs to produce brighter light while utilizing less power, thereby improving overall energy efficiency. Consequently, the dual challenges of optimizing the peak emission wavelength and achieving a narrow FWHM continue to present significant obstacles in the field of molecular engineering.

To precisely regulate the emission spectra for pure-red emission and achieve high EL performance, herein, we propose a strategy to enhance π-conjugation and extend FMO delocalization. Specifically, the incorporation of a dibenzo[*c*,*g*]carbazole (BCz) unit into a para boron/oxygen-embedded framework effectively enhances π-conjugation and extends the delocalization of FMOs, enabling precise tuning of the emission peak position to achieve pure-red emission. Importantly, this approach avoids the unpredictable spectral shifts and molecular weight increase by introducing additional push–pull electron (atom) groups, providing an effective molecular paradigm for achieving long-wavelength MR-TADF materials with narrowband emission. We synthesized three new compounds, **PhCzBN**, **PhBCzBN**, and **BCzBN**, by progressively replacing 3,6-diphenyl-9*H*-carbazole (PhCz) with 7*H*-dibenzo[*c*,*g*]carbazole (BCz) fragments. These compounds exhibited progressively red-shifted emission peaks, ranging from 609 to 631 nm in toluene, while maintaining narrow emission linewidths. Moreover, the **BCzBN**-based device showed a high EQE_{max} of 33.8% and CIE coordinates of (0.700, 0.300), close to the BT.2020 requirements (Scheme 1).

Results and discussion

Synthesis and electrochemical properties

The synthetic routes for **PhCzBN**, **PhBCzBN**, and **BCzBN** are shown in Scheme S1.† The borylation precursors were prepared through nucleophilic substitution reactions using well-established intermediates, specifically 4,4′-((2,5-dibromo-3,6-difluoro-1,4-phenylene)bis(oxy))bis(tert-butylbenzene), along with the corresponding nucleophilic reagents, 3,6-diphenyl-9*H*-carbazole and 7*H*-dibenzo[*c*,*g*]carbazole fragments. Notably, the precursor for the asymmetrical **PhBCzBN** was obtained *via* a one-pot method, using an equimolar mixture of PhCz and BCz.[14] The final products, **PhCzBN**, **PhBCzBN**, and **BCzBN**, were synthesized through a lithium–chloride exchange reaction with *t*-BuLi, followed by electrophilic trapping with BBr_3, and then an electrophilic aromatic borylation reaction in the presence of diisopropylethylamine.[10,15] All new compounds were fully characterized using ^1H and ^{13}C NMR spectroscopy (Fig. S2–S10†), and the final products were further validated using high-resolution mass spectrometry (HR-MS) (Fig. S11–S13†). Thermogravimetric analysis (TGA) demonstrated the excellent thermal stability of these compounds, with high decomposition temperatures (T_d, corresponding to 5 wt% loss) of 484 °C for **PhCzBN**, 485 °C for **PhBCzBN**, and 487 °C for **BCzBN** (Fig. S14†). This high thermal stability is advantageous for sublimation purification and device fabrication. To elucidate the electrochemical properties of these compounds, cyclic voltammetry (CV) measurements were conducted with a conventional three-electrode system. As shown in Fig. S15,† the highest occupied molecular orbital energy levels (E_{HOMO}) of **PhCzBN**, **PhBCzBN**, and **BCzBN** are estimated to be −4.99 eV, −5.07 eV, and −5.19 eV, respectively. Based on the optical bandgaps (E_gs), derived from the onset of the absorption spectra (2.01 eV for **PhCzBN**, 1.98 eV for **PhBCzBN**, and 1.96 eV for **BCzBN**), the lowest unoccupied molecular orbital energy levels (E_{LUMO}) are calculated to be −2.98 eV, −3.09 eV, and −3.23 eV, respectively. A single crystal of **BCzBN** was grown from a methanol/dichloromethane mixture and subjected to X-ray crystallographic analysis (Fig. 1b and Table S1†). As illustrated in Fig. 1b, the single crystal structure reveals a highly distorted configuration of the B,N,B-embedded hetero[5]helicene blade fused with the central MR framework. The dimensions of **BCzBN** are

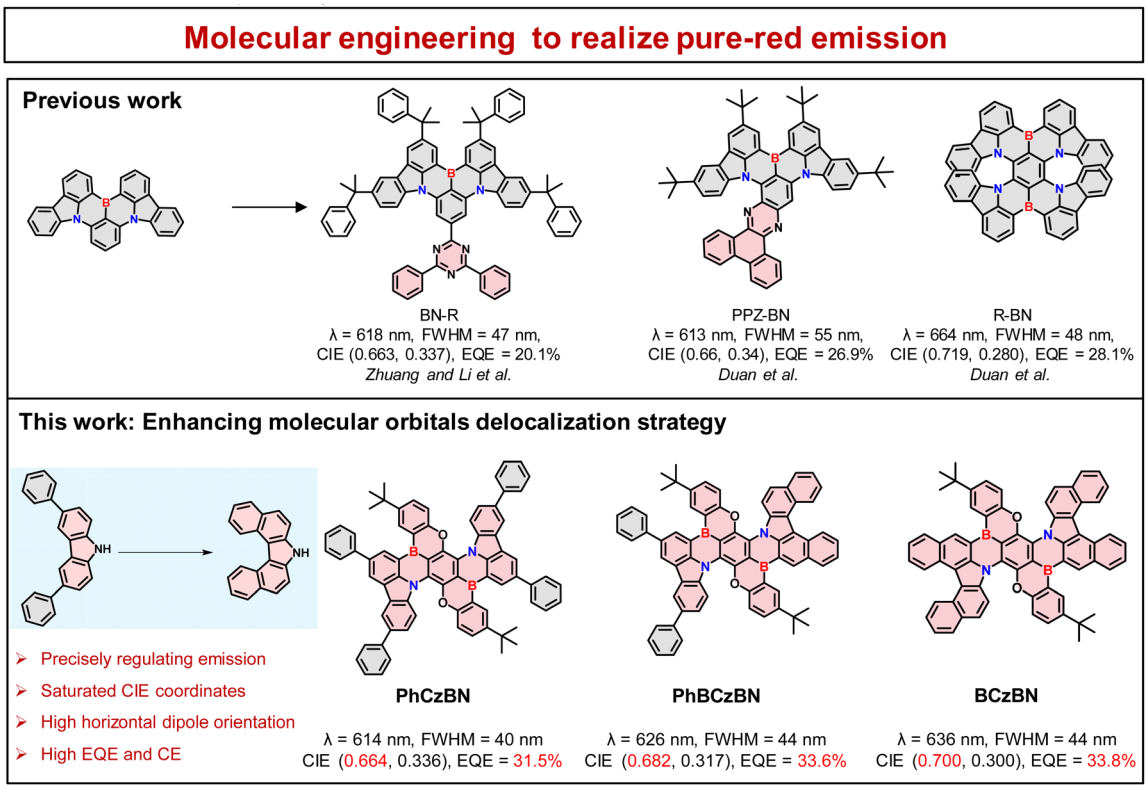

Scheme 1 Design strategy and chemical structures of this work.

approximately 18.73 Å in length and 18.29 Å in width, with a dihedral angle of only 14° between planes A and B. Enantiomeric pairs were identified in the packing pattern, consistent with the observation of a single set of signals in its NMR spectrum. The racemic dimers are alternately stacked to form a columnar arrangement. Furthermore, the racemization

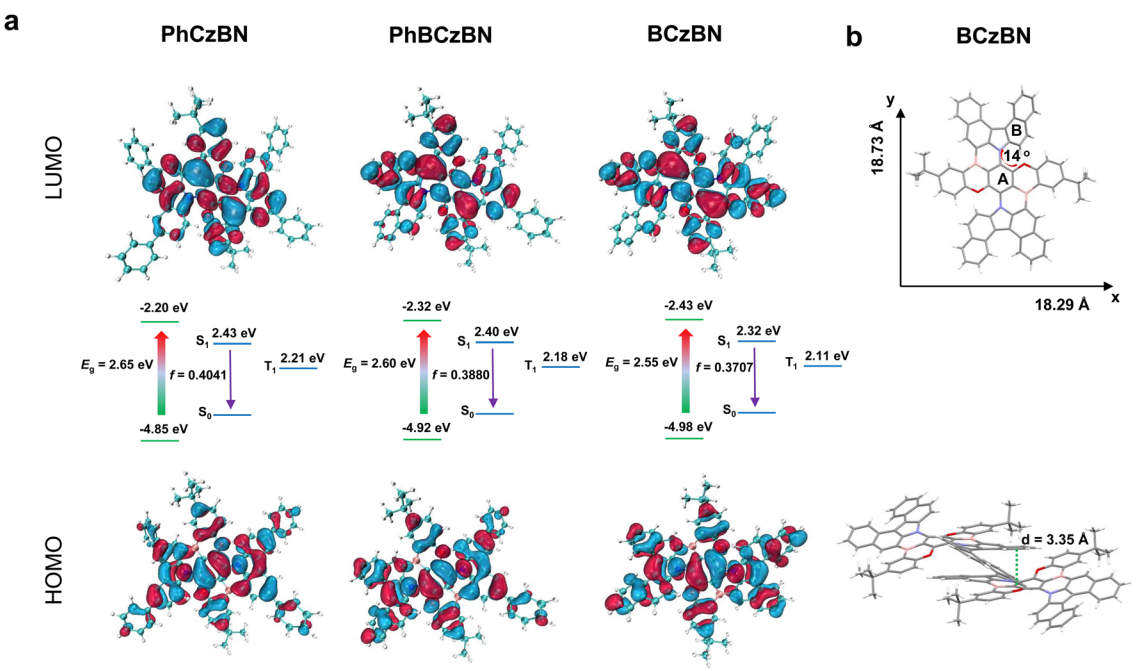

Fig. 1 (a) Theoretical calculated results of **PhCzBN**, **PhBCzBN**, and **BCzBN** (DFT and TD-DFT were performed based on the B3LYP density functional method with the basis set 6-31G(d, p); the S_1 and T_1 energy values were calculated by SCS-CC2 using the MRCC Program with the cc-PVDZ method). (b) Single-crystal structure of **BCzBN** and its stacking model.

barriers of the enantiomers were calculated, revealing activation barriers for the helical inversion process of $\Delta G^{\ddagger}$ = 10.9 kcal mol^{-1}, which underscores the considerable stability of the racemic form. In terms of packing pattern, **BCzBN** displays a head-to-tail molecular arrangement with a short π–π distance, indicating strong intermolecular interactions. The incorporation of the large BCz moiety induces a more rigid and large configuration, promoting a high horizontal ratio of emitting dipole orientation ($\theta_{\parallel}$) and contributing to a red shift in the emission spectrum.

Theoretical calculation

To better explore the underlying mechanisms of the π-conjugation extension effect on the electronic characteristics and geometrical differences of the three new compounds, density functional theory (DFT) calculations were performed to optimize the ground states using Gaussian 09 with a 6-31G(d,p) basis set. As depicted in Fig. 1a, the computational results reveal two critical insights. First, similar to conventional MR-TADF materials, the three compounds display atomically separated FMOs within the core of the MR-TADF skeleton. The LUMOs are predominantly situated on the boron atoms and at their *ortho* and *para* positions, while the HOMOs are fundamentally distributed over the nitrogen atoms and the meta positions of the boron atoms. This alternating pattern of HOMOs and LUMOs promotes SR-CT, leading to TADF behavior. Second, there is a notable migration of HOMO and LUMO distributions toward the BCz segments, progressing from **PhCzBN** to **PhBCzBN** to **BCzBN**. This migration results from the extended π-extension provided by the embedded BCz segments, which has been demonstrated as an effective strategy for modifying the emission peaks, FWHMs, and spectral shapes of red emitters. The optical bandgap (E_g) values of the three emitters, 2.65 eV, 2.60 eV, and 2.55 eV, respectively, aligned well with the observed spectral variations. These findings confirm the feasibility of increasing the BCz segment in the fusion strategy to achieve red-shifted emission.

Photophysical properties

The photophysical properties of **PhCzBN**, **PhBCzBN**, and **BCzBN** in toluene were measured, and the results are summarized in Fig. 2 and Table 1. As shown in Fig. 2a, all compounds display multiple absorption bands within the 300–650 nm range, with a pronounced absorption peak around 600 nm, attributed to π–π* transitions and SR-CT. The steady-state fluorescence (Fl.) spectra were recorded in dilute toluene (1×10^{-5} M) at room temperature. The three emitters exhibit narrowband emission peaks at 609, 623, and 631 nm with FWHM values of 32 nm (0.11 eV), 37 nm (0.12 eV), and 37 nm (0.12 eV), respectively. Weak shoulder peaks were observed at 656, 670, and 680 nm compared to the primary emission peaks. To understand the variation of spectral profiles for **PhCzBN**, **PhBCzBN**, and **BCzBN**, the vibrationally resolved emission spectra and Huang–Rhys factor were simulated using the Molecular Materials Property Prediction Package software (Fig. S18†). All three compounds exhibited similar vibrational modes. Their Huang–Rhys factors were tiny and mainly contributed to vibrations coupling at low frequencies, while high-frequency vibrations were negligible. The simulated fluorescence spectra of the three emitters exhibited a narrow primary peak and a weak shoulder peak, with FWHM values of 784 cm^{-1}, 971 cm^{-1}, and 1062 cm^{-1}, respectively. The narrow FWHMs and weak shoulder peaks demonstrate the effectiveness of the molecular design strategy in mitigating vibrational coupling and structural relaxation during the radiative process. The singlet (S_1) and triplet (T_1) energies were estimated from low-temperature fluorescence and phosphorescence spectra in toluene at 77 K (Fig. S20†). The S_1/T_1 energy values are 2.10/1.85 eV, 2.08/1.85 eV, and 2.05/1.82 eV, respectively. Consequently, the ΔE_{ST} values of the three compounds are calculated to be 0.25 eV, 0.23 eV, and 0.23 eV, respectively.

The photophysical properties of **PhCzBN**, **PhBCzBN**, and **BCzBN** in the film state were investigated using 1 wt% doped 5-(3-(4,6-diphenyl-1,3,5-triazin-2-yl)phenyl)-7,7-dimethyl-5,7-dihydroin deno [2,*1-b*]carbazole (DMIC-TRZ).[16] All three compounds manifest spectral shapes similar to those observed in toluene solution (Fig. 2b). The maximum emission peaks for **PhCzBN**, **PhBCzBN**, and **BCzBN** are at 614 nm, 627 nm, and 636 nm, with corresponding FWHM values of 35 nm (0.12 eV), 41 nm (0.13 eV), and 41 nm (0.13 eV), respectively. The slightly red-shifted and broadened emission profiles in the film state are attributed to the enhanced intermolecular interactions. These films exhibit high ϕ_{PL} of 90% for **PhCzBN**, 92% for **PhBCzBN**, and 94% for **BCzBN**. To investigate the TADF behaviors of the three emitters, transient photoluminescence spectra were monitored in 1 wt% doped DMIC-TRZ films at 300 K. As shown in Fig. 2c, all three emitters exhibit clear second-order exponential behaviors, with a nanosecond prompt component and a millisecond delayed component. The prompt fluorescence lifetimes and delayed fluorescence lifetimes are 12.4 ns/0.91 ms, 8.3 ns/0.82 ms, and 5.7 ns/0.68 ms for **PhCzBN**, **PhBCzBN**, and **BCzBN**, respectively. The prolonged delayed fluorescence lifetimes indicate weak TADF characteristics and low exciton utilization. The rigid molecular skeletons and short fluorescence lifetimes of these emitters result in high radiative decay rates of 7.3×10^7 s^{-1} for **PhCzBN**, 1.1×10^8 s^{-1} for **PhBCzBN**, and 1.6×10^8 s^{-1} for **BCzBN**. These rates exceed the corresponding non-radiative decay rate constants (k_{nr}), which are 8.1×10^6 s^{-1} for **PhCzBN**, 8.3×10^6 s^{-1} for **PhBCzBN**, and 1.4×10^7 s^{-1} for **BCzBN**. Furthermore, the extended π-extension of the three emitters provided a significant degree of anisotropy, resulting in high $\theta_{\parallel}$, as revealed by the angle-dependent polarized photoluminescence spectra (Fig. S26†). Such high $\theta_{\parallel}$ could have a favorable influence on the optical out-coupling factor, thereby improving the EL performance.

Electroluminescence properties

Inspired by the fine-tuned PL spectra and high ϕ_{PL}s, multilayer OLEDs using **PhCzBN**, **PhBCzBN**, and **BCzBN** as terminal emitters were fabricated by vacuum deposition with the following optimized configuration of ITO/HAT-CN (5 nm)/TAPC (30 nm)/TCTA (15 nm)/mCBP (10 nm)/emitting layer (EML)/PO-

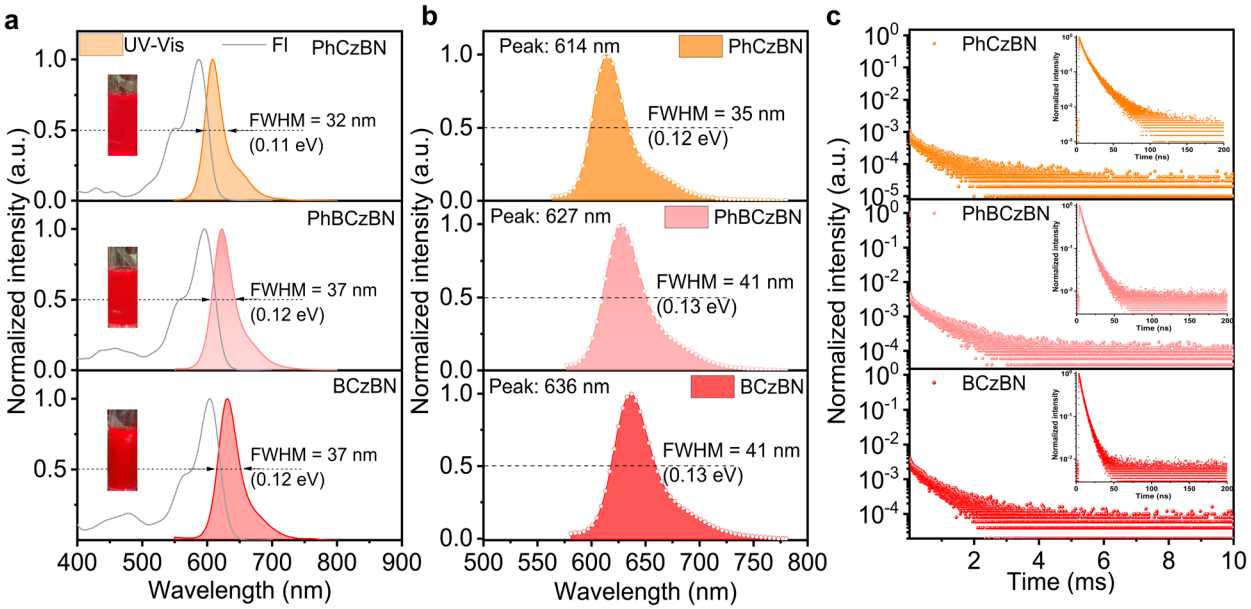

Fig. 2 (a) UV-visible absorption (UV-vis) and fluorescence (Fl.) spectra of **PhCzBN**, **PhBCzBN**, and **BCzBN** in toluene (1×10^{-5} mol L^{-1}) at 300 K. (b) Fl. spectra measured in DMIC-TRZ film. (c) Transient photoluminescence spectra recorded in DMIC-TRZ film.

T2T (20 nm)/ANT-BIZ (30 nm)/Liq (2 nm)/Al (100 nm). In the device configuration, dipyrazino[2,3-*f*:2′,3′-*h*]quinoxaline-2,3,6,7,10,11-hexacarbonitrile (HAT-CN) was used as a hole-injection layer; 1,1-bis((di-4-tolylamino)phenyl)-cyclohexane (TAPC) and (1-(4-(10-([1,1′-biphenyl]-4-yl)anthracen-9-yl) phenyl)-2-ethyl-1*H*-benzo[*d*]-imidazole) (ANT-BIZ) were employed as hole- and electron-transport layers, respectively; 1,3-di(9*H*-carbazol-9-yl)benzene (mCBP) and oxybis(2,1-phenylene))bis(diphenylphosphine oxide (PO-T2T) served as exciton-blocking layers; and 8-hydroxyquinolinolato-lithium (Liq) and Al were the electron-injection layer and cathode, respectively. Due to its superior charge-carrying mobility, DMIC-TRZ was selected as the host in the emitting layer. The proposed emitters were doped into the host at optimal doping concentrations of 1 wt% to reduce unwanted exciton trapping. The chemical structures and energy level diagram of all functional layers, electroluminescence characteristics, and summarized device performance are provided in Fig. S27 and S28.†

The devices incorporating these emitters exhibited pure-red emission, with peak wavelengths at 612 nm for **PhCzBN**, 627 nm for **PhBCzBN**, and 636 nm for **BCzBN**, with FWHMs of 36 nm, 42 nm, and 42 nm, respectively. These results validate the efficacy of our molecular design strategy for red-shifting the emission spectrum by progressively extending molecular conjugation. The EQE_{max} values of the devices were 12.2% for **PhCzBN**, 18.4% for **PhBCzBN**, and 13.9% for **BCzBN**. The suboptimal EQE_{max} values could be attributed to prolonged delayed lifetimes and limited TADF characteristics.

To further enhance EL performance and minimize efficiency roll-off, we employed the phosphorescent sensitizer of $Ir(mphmq)_2tmd$ to facilitate the recycling of triplet excitons under electrical excitation.[17] The sensitized emission mechanism involves efficiently harvesting triplet excitons with the sensitizer and subsequently transferring them to the terminal emitter. Given the low emitter doping concentration of 1 wt%, Dexter energy transfer could be negligible, making Förster resonance energy transfer (FRET) the predominant process in the sensitized system.[18] Consequently, the EML configuration of the sensitized devices was formulated as 79 wt% DMIC-TRZ, 20 wt% $Ir(mphmq)_2tmd$, and 1 wt% emitter. The photoluminescence spectrum of $Ir(mphmq)_2tmd$ aligns well with the

Table 1 Physical data of **PhCzBN**, **PhBCzBN**, and **BCzBN**

Emitter	λ_{abs}[a] [nm]	λ_{em}[a] [nm]	FWHM[a] [nm]	E_{S1}[b] [eV]	E_{T1}[c] [eV]	ΔE_{ST}[d] [eV]	E_{HOMO}[e] [eV]	E_{LUMO}[f] [eV]	T_d[g] [°C]	$\theta_{\parallel}$[h] [%]
PhCzBN	590	609	32	2.10	1.85	0.25	−4.99	−2.98	484	91.7
PhBCzBN	596	623	37	2.08	1.85	0.23	−5.07	−3.09	485	98.8
BCzBN	605	631	37	2.05	1.82	0.23	−5.19	−3.23	487	99.6

[a] Measured in dilute toluene at 300 K (1×10^{-5} M). [b] Estimated from the onset of the Fl. spectra in toluene at 77 K. [c] Estimated from the onset of the Phos. spectra in toluene at 77 K. [d] Calculated from the formula $\Delta E_{ST} = E_{S1} - E_{T1}$. [e] Determined in a dichloromethane solution containing 0.1 M of tetrabutylammonium hexafluorophosphate (n-Bu_4NPF_6). [f] Estimated from the formula $E_{LUMO} = E_{HOMO} - E_g$. [g] Thermal decomposition temperatures (T_d) were determined by the recorded temperature at 5% weight loss. [h] Horizontal ratio of emitting dipole orientation ($\theta_{\parallel}$) measured in DMIC-TRZ film.

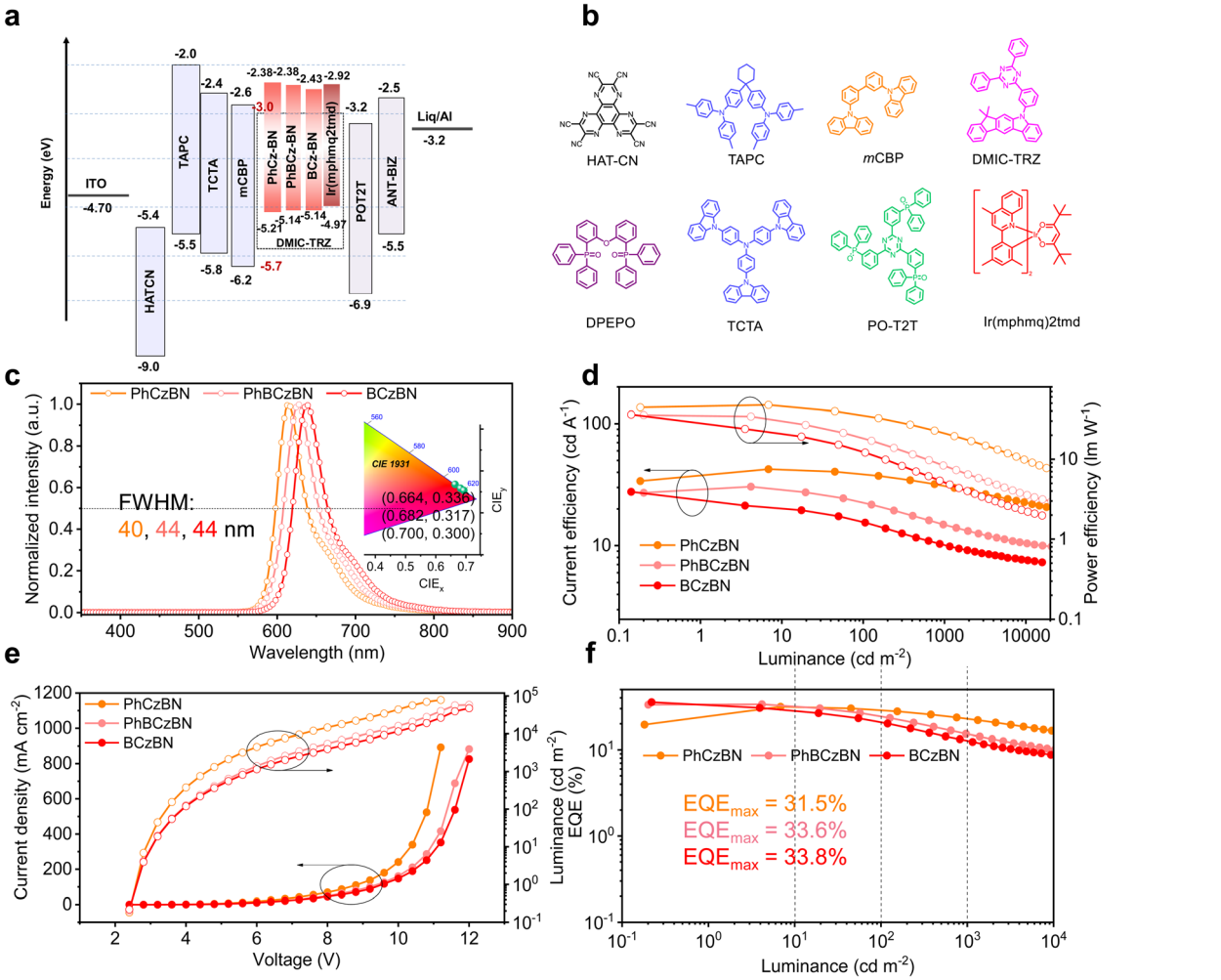

Fig. 3 Electroluminescence properties of the sensitized devices based on **PhCzBN**, **PhBCzBN**, and **BCzBN**. (a) Device architecture and energy level diagram of functional materials. (b) Chemical structures of organic functional materials. (c) EL spectra. (d) Current efficiency and power efficiency *versus* luminance plots. (e) Current density and luminance *versus* voltage characteristics. (f) External quantum efficiency *versus* luminance curves.

absorption spectra of all three emitters (Fig. S30†), ensuring efficient energy transfer from the sensitizer to the terminal emitters. The device configuration, energy level diagrams, and chemical structures of functional materials are illustrated in Fig. 3.

As shown in Fig. 3b, all devices demonstrate efficient carrier injection and transport, with turn-on voltages as low as 2.6 V (at 1 cd m^{-2}) during electrical excitation. At 1 wt% doping concentration, the three emitters achieve effective energy transfer, resulting in pure-red emission with peaks at 614 nm, 626 nm, and 636 nm, and FWHMs of 40 nm (0.13 eV), 44 nm (0.14 eV), and 44 nm (0.14 eV) for **PhCzBN**, **PhBCzBN**, and **BCzBN**, respectively. These narrow spectral profiles and optimal peak positions yield CIE coordinates of (0.664, 0.336), (0.682, 0.317), and (0.700, 0.300), respectively. It is noted that the CIE coordinates of the **BCzBN**-based device closely align with the BT.2020 standards for the red gamut.

Aside from excellent color purity, all sensitized devices exhibit outstanding EL performance (Fig. 3d–f, 4a and Table 2). The introduction of a sensitizer significantly enhances the maximum luminance (L_{max}) of the devices, reaching 78 590 cd m^{-2} for **PhCzBN**, 57 971 cd m^{-2} for **PhBCzBN**, and 46 568 cd m^{-2} for **BCzBN**, respectively. Furthermore, these devices demonstrate remarkable EQE_{max} of 31.5%, 33.6%, and 33.8%, respectively. The maximum current efficiencies (CE_{max}) and maximum power efficiencies (PE_{max}) were 42.5 cd A^{-1}/47.6 lm W^{-1} for **PhCzBN**, 30.5 cd

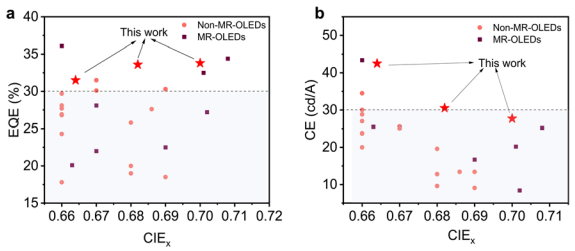

Fig. 4 (a) EQE *versus* CIE_x plots of representative red OLEDs (CIE_x > 0.66). (b) CE *versus* CIE_x plots of representative red OLEDs (CIE_x > 0.66).

Table 2 Summary of the key device performance for the red OLEDs

Emitter	V_{on}[a] [V]	λ_{EL}[b] [nm]	L_{max}[c] [cd m^{-2}]	CE_{max}[d] [cd A^{-1}]	PE_{max}[e] [lm W^{-1}]	EQE[f] [%] max/100/1000	FWHM[g] [nm eV^{-1}]	CIE[h] [x, y]
PhCzBN	2.6	614	78 590	42.5	47.6	31.5/28.6/23.0	40/0.13	(0.664, 0.336)
PhBCzBN	2.6	626	57 971	30.5	35.6	33.6/24.3/15.4	44/0.14	(0.682, 0.317)
BCzBN	2.6	636	46 568	27.7	36.2	33.8/20.2/12.5	44/0.14	(0.700, 0.300)

[a] Turn-on voltage recorded at a luminance of 1 cd m^{-2}. [b] Maximum EL wavelength. [c] Maximum brightness. [d] Maximum current efficiency. [e] Maximum power efficiency. [f] Maximum external quantum efficiency at 100 cd m^{-2}/1000 cd m^{-2}. [g] FWHM of EL spectra. [h] CIE coordinates.

A^{-1}/35.6 lm W^{-1} for **PhBCzBN**, and 27.7 cd A^{-1}/36.2 lm W^{-1} for **BCzBN**. The favorable spectral positions and narrow emission peaks help minimize the proportion of near-infrared (NIR) components above 700 nm, resulting in significantly improved CE_{max} compared to previously reported OLEDs (Fig. 4b and Table S3†). The exceptional EL performance is attributed to the high ϕ_{PL}, preferential $\theta_{\parallel}$ of the emitters, and effective FRET transfer. Additionally, the high exciton utilization through the sensitization process also reduces efficiency roll-off compared to non-sensitized devices. For instance, the device based on **PhCzBN** maintains an EQE of 28.6% at 100 cd m^{-2} and 23.0% at 1000 cd m^{-2}, indicating efficiency roll-offs of 9.2% and 26.9%, respectively. The improved efficiency roll-off observed in **PhBCzBN** and **BCzBN** devices is likely due to their extended molecular skeletons and planar configurations, which enhance triplet–triplet and singlet–triplet annihilation processes.

Conclusions

We have successfully designed and synthesized three new pure-red MR-TADF emitters, **PhCzBN**, **PhBCzBN**, and **BCzBN**, through a stepwise extension of molecular conjugation. These emitters feature narrow bandwidths, high ϕ_{PL}s, and excellent horizontal dipole ratios. Leveraging their superior photophysical properties and optimized device configurations, the sensitized devices have shown exceptional electroluminescent performance. Notably, **PhBCzBN**-based devices achieved an impressive EQE_{max} of 33.6%, a CE_{max} of 30.5 cd A^{-1}, and a narrow FWHM of 44 nm (0.14 eV). Furthermore, the **BCzBN**-based device achieved the highest EQE_{max} of 33.8% with notable CIE coordinates of (0.700, 0.300), closely matching the BT.2020 standard for red color. This study paves the way for future commercial applications of high-performance TADF emitters and advancements in wide color gamut display technologies.

Data availability

All data supporting this study are available in the ESI.† Additional data are available from the corresponding author upon reasonable request.

Author contributions

X. Wang and T. Hua synthesized the emitters and characterized the photophysical property. N. Li, G. Chen, and J. Miao fabricated and characterized the OLED devices. Z. Chen provided guidance on theoretical calculations. T. Hua wrote the manuscript. X. Cao provided suggestions on experiments. C. Yang supervised and directed this study.

Conflicts of interest

There are no conflicts to declare.

Acknowledgements

This work was supported by the National Natural Science Foundation of China (52130308 and 22405177), Shenzhen Science and Technology Program (JCYJ20220818095816036 and ZDSYS20210623091813040), and Guangdong Basic and Applied Basic Research Foundation (2022A1515110874). We thank the Instrumental Analysis Center of Shenzhen University for analytical support.

Notes and references

1 (*a*) N. Thejo Kalyani and S. J. Dhoble, *Renewable Sustainable Energy Rev.*, 2012, **16**, 2696–2723; (*b*) K. Guo, Z. Tang, X. Chou, S. Pan, C. Wan, T. Xue, L. Ding, X. Wang, J. Huang, F. Zhang and B. Wei, *Advanced Photonics Nexus*, 2023, **2**, 044001.

2 (*a*) X. Fan, X. Hao, F. Huang, J. Yu, K. Wang and X. Zhang, *Adv. Sci.*, 2023, **10**, 2303504; (*b*) C.-L. Lin, P.-S. Chen, M.-Y. Deng, C.-E. Wu, W.-C. Chiu and Y.-S. Lin, *IEEE J. Electron Devices Soc.*, 2018, **6**, 26–33; (*c*) T. Hua, X. Cao, J. Miao, X. Yin, Z. Chen, Z. Huang and C. Yang, *Nat. Photon.*, 2024, **18**, 1161–1169.

3 (*a*) A. Khan, X. Tang, C. Zhong, Q. Wang, S. Y. Yang, F. C. Kong, S. Yuan, A. S. D. Sandanayaka, C. Adachi, Z. Q. Jiang and L. S. Liao, *Adv. Funct. Mater.*, 2021, **31**, 2009488; (*b*) Z. G. Wu, Y. Xin, C. Lu, W. Huang, H. Xu, X. Liang, X. Cao, C. Li, D. Zhang, Y. Zhang and L. Duan, *Angew. Chem., Int. Ed.*, 2024, **63**, e202318742.

4 (*a*) T. Hatakeyama, K. Shiren, K. Nakajima, S. Nomura, S. Nakatsuka, K. Kinoshita, J. Ni, Y. Ono and T. Ikuta, *Adv. Mater.*, 2016, **28**, 2777–2781; (*b*) Y. Kondo, K. Yoshiura, S. Kitera, *et al.*, *Nat. Photon.*, 2019, **13**, 678–682; (*c*) M. Mamada, M. Hayakawa, J. Ochi and T. Hatakeyama, *Chem. Soc. Rev.*, 2024, **53**, 1624–1692; (*d*) Y. Sano, T. Shintani, M. Hayakawa, S. Oda, M. Kondo, T. Matsushita and T. Hatakeyama, *J. Am. Chem. Soc.*, 2023, **145**, 11504–11511; (*e*) H. Tanaka, S. Oda, G. Ricci, H. Gotoh, K. Tabata, R. Kawasumi, D. Beljonne, Y. Olivier and T. Hatakeyama, *Angew. Chem., Int. Ed.*, 2021, **60**,

17910–17914; (*f*) G. Meng, H. Dai, J. Zhou, T. Huang, X. Zeng, Q. Wang, X. Wang, Y. Zhang, T. Fan, D. Yang, D. Ma, D. Zhang and L. Duan, *Chem. Sci.*, 2023, **14**, 979–986.

5 (*a*) X.-C. Fan, F. Huang, H. Wu, H. Wang, Y.-C. Cheng, J. Yu, K. Wang and X.-H. Zhang, *Angew. Chem., Int. Ed.*, 2023, **62**, e202305580; (*b*) T. Hua, J. Miao, H. Xia, Z. Huang, X. Cao, N. Li and C. Yang, *Adv. Funct. Mater.*, 2022, **32**, 2201032; (*c*) X. Qiu, G. J. Tian, C. W. Lin, Y. Y. Pan, X. Y. Ye, B. H. Wang, D. G. Ma, D. H. Hu, Y. Luo and Y. G. Ma, *Adv. Optical Mater.*, 2021, **9**, 2001845; (*d*) T. Huang, L. Yuan, X. Lu, Y. Qu, C. Qu, Y. Xu, Y.-X. Zheng and Y. Wang, *Chem. Sci.*, 2024, **15**, 15170.

6 (*a*) S. Madayanad Suresh, D. Hall, D. Beljonne, Y. Olivier and E. Zysman-Colman, *Adv. Funct. Mater.*, 2020, **30**, 1908677; (*b*) D. Hall, S. M. Suresh, P. L. dos Santos, E. Duda, S. Bagnich, A. Pershin, P. Rajamalli, D. B. Cordes, A. M. Z. Slawin, D. Beljonne, A. Köhler, I. D. W. Samuel, Y. Olivier and E. Zysman-Colman, *Adv. Optical Mater.*, 2020, **8**, 1901627; (*c*) H. J. Kim and T. Yasuda, *Adv. Optical Mater.*, 2022, **10**, 2201714; (*d*) J.-M. Teng, Y.-F. Wang and C.-F. Chen, *J. Mater. Chem. C*, 2020, **8**, 11340–11353.

7 (*a*) C. Cao, J. H. Tan, Z. L. Zhu, J. D. Lin, H. J. Tan, H. Chen, Y. Yuan, M. K. Tse, W. C. Chen and C. S. Lee, *Angew. Chem., Int. Ed.*, 2023, **135**, e202215226; (*b*) X. Wang, L. Wang, G. Meng, X. Zeng, D. Zhang and L. Duan, *Sci. Adv.*, 2023, **9**, eadh1434.

8 (*a*) S. Uemura, S. Oda, M. Hayakawa, R. Kawasumi, N. Ikeda, Y.-T. Lee, C.-Y. Chan, Y. Tsuchiya, C. Adachi and T. Hatakeyama, *J. Am. Chem. Soc.*, 2022, **145**, 1505–1511; (*b*) J. Liu, Y. Zhu, T. Tsuboi, C. Deng, W. Lou, D. Wang, T. Liu and Q. Zhang, *Nat. Commun.*, 2022, **13**, 4876; (*c*) Y.-T. Lee, C.-Y. Chan, N. Matsuno, S. Uemura, S. Oda, M. Kondo, R. W. Weerasinghe, Y. Hu, G. N. I. Lestanto, Y. Tsuchiya, Y. Li, T. Hatakeyama and C. Adachi, *Nat. Commun.*, 2024, **15**, 3174; (*d*) X.-C. Fan, K. Wang, Y.-Z. Shi, Y.-C. Cheng, Y.-T. Lee, J. Yu, X.-K. Chen, C. Adachi and X.-H. Zhang, *Nat. Photon.*, 2023, **17**, 280–285; (*e*) S. Madayanad Suresh, L. Zhang, D. Hall, C. Si, G. Ricci, T. Matulaitis, A. M. Z. Slawin, S. Warriner, Y. Olivier, I. D. W. Samuel and E. Zysman-Colman, *Angew. Chem., Int. Ed.*, 2023, **62**, e202215522; (*f*) J. Ochi, Y. Yamasaki, K. Tanaka, Y. Kondo, K. Isayama, S. Oda, M. Kondo and T. Hatakeyama, *Nat. Commun.*, 2024, **15**, 2361; (*g*) I. S. Park, M. Yang, H. Shibata, N. Amanokura and T. Yasuda, *Adv. Mater.*, 2022, **34**, 2107951.

9 (*a*) H. Chen, T. Fan, G. Zhao, D. Zhang, G. Li, W. Jiang, L. Duan and Y. Zhang, *Angew. Chem., Int. Ed.*, 2023, **135**, e202300934; (*b*) X. L. Cai, Y. C. Xu, Y. Pan, L. J. Li, Y. X. Pu, X. M. Zhuang, C. L. Li and Y. Wang, *Angew. Chem., Int. Ed.*, 2023, **62**, e202216473; (*c*) A. T. Gogoulis, R. Hojo, K. Bergmann and Z. M. Hudson, *Org. Lett.*, 2023, **25**, 7791–7795; (*d*) X. C. Fan, K. Wang, Y. Z. Shi, J. X. Chen, F. Huang, H. Wang, Y. N. Hu, Y. Tsuchiya, X. M. Ou, J. Yu, C. Adachi and X. H. Zhang, *Adv. Optical Mater.*, 2022, **10**, 2101789; (*e*) K. R. Naveen, S. J. Hwang, H. Lee and J. H. Kwon, *Adv. Electron. Mater.*, 2022, **8**, 2101114.

10 Y. W. Zhang, D. D. Zhang, T. Y. Huang, A. J. Gillett, Y. Liu, D. P. Hu, L. S. Cui, Z. Y. Bin, G. M. Li, J. B. Wei and L. Duan, *Angew. Chem., Int. Ed.*, 2021, **60**, 20498–20503.

11 M. Yang, I. S. Park and T. Yasuda, *J. Am. Chem. Soc.*, 2020, **142**, 19468–19472.

12 T. J. Fan, M. X. Du, X. Q. Jia, L. Wang, Z. Yin, Y. L. Shu, Y. W. Zhang, J. B. Wei, D. D. Zhang and L. Duan, *Adv. Mater.*, 2023, **35**, e2301018.

13 (*a*) Y. Zou, J. Hu, M. Yu, J. Miao, Z. Xie, Y. Qiu, X. Cao and C. Yang, *Adv. Mater.*, 2022, **34**, e2201442; (*b*) T. Hua, N. Li, Z. Huang, Y. Zhang, L. Wang, Z. Chen, J. Miao, X. Cao, X. Wang and C. Yang, *Angew. Chem., Int. Ed.*, 2024, **63**, e202318433; (*c*) J. He, Y. Xu, S. Luo, J. Miao, X. Cao and Y. Zou, *Chem. Eng. J.*, 2023, **471**, 144565; (*d*) Y. Zou, J. He, N. Li, Y. Hu, S. Luo, X. Cao and C. Yang, *Mater. Horiz.*, 2023, **10**, 3712–3718.

14 Y. Y. Jing, N. Q. Li, X. S. Cao, H. Wu, J. S. Miao, Z. X. Chen, M. L. Huang, X. Z. Wang, Y. X. Hu, Y. Zou and C. L. Yang, *Sci. Adv.*, 2023, **9**, eadh8296.

15 (*a*) H. Hirai, K. Nakajima, S. Nakatsuka, K. Shiren, J. Ni, S. Nomura, T. Ikuta and T. Hatakeyama, *Angew. Chem., Int. Ed.*, 2015, **54**, 13581–13585; (*b*) T. Hua, L. S. Zhan, N. Q. Li, Z. Y. Huang, X. S. Cao, Z. Q. Xiao, S. L. Gong, C. J. Zhou, C. Zhong and C. L. Yang, *Chem. Eng. J.*, 2021, **426**, 131169.

16 D. Zhang, C. Zhao, Y. Zhang, X. Song, P. Wei, M. Cai and L. Duan, *ACS Appl. Mater. Interfaces*, 2017, **9**, 4769–4777.

17 (*a*) D. H. Kim, N. S. Cho, H.-Y. Oh, J. H. Yang, W. S. Jeon, J. S. Park, M. C. Suh and J. H. Kwon, *Adv. Mater.*, 2011, **23**, 2721–2726; (*b*) U. Deori, G. P. Nanda, C. Murawski and P. Rajamalli, *Chem. Sci.*, 2024, **15**, 17739–17759.

18 (*a*) L. Zhan, A. Ying, Y. Qi, K. Wu, Y. Tang, Y. Tan, Y. Zou, G. Xie, S. Gong and C. Yang, *Adv. Funct. Mater.*, 2021, **31**, 2106345; (*b*) J. Yan, S. F. Wang, C.-H. Hsu, E. H.-C. Shi, C.-C. Wu, P.-T. Chou, S.-M. Yiu, Y. Chi, C. You, I. C. Peng and W.-Y. Hung, *ACS Appl. Mater. Interfaces*, 2023, **15**, 21333–21343.